Supplemental Document

Optics EXPRESS

Fast and rigorous optical simulation of periodically corrugated light-emitting diodes based on a diffraction matrix method: supplement

CHANHYUNG PARK,[1,†] JEONGMIN SHIN,[1,†] SANMUN KIM,[1] SONGJU LEE,[1] JUHO PARK,[1] JAEHYEOK PARK,[1] SEHONG PARK,[2] SEUNGHYUP YOO,[1,3] AND MIN SEOK JANG[1,4,]

[1] *School of Electrical Engineering, Korea Advanced Institute of Science and Technology, 34141 Daejeon, Republic of Korea*
[2] *OC Optical Technology Task, LG Display, 07796 Seoul, Republic of Korea*
[3] *syoo_ee@kaist.ac.kr*
[4] *jang.minseok@kaist.ac.kr*
[†] *These authors contributed equally to this work*

Supplement DOI: https://doi.org/10.6084/m9.figshare.22811681

Parent Article DOI: https://doi.org/10.1364/OE.489758

Supplementary document for: Fast and rigorous optical simulation of periodically corrugated light-emitting diodes based on a diffraction matrix method

CHANHYUNG PARK [1,†], JEONGMIN SHIN [1,†], SANMUN KIM[1], SONGJU LEE[1], JUHO PARK[1], JAEHYEOK PARK[1], SEHONG PARK[2], SEUNGHYUP YOO[1,3,*], AND MIN SEOK JANG[1,4,*]

[1]*School of Electrical Engineering, Korea Advanced Institute of Science and Technology, 34141 Daejeon, Korea*
[2]*OC Optical Technology Task, LG Display, 07796 Seoul, Korea*
[3] *syoo_ee@kaist.ac.kr*
[4] *jang.minseok@kaist.ac.kr*

[†] *These authors contributed equally to this work*

S1. Derivation of complex electric field amplitude

To calculate the complex amplitude of plane waves at the top surface, we should first consider the decomposed plane waves emitted from the dipole. The emission of a light-emitting dipole with dipole moment p_0 in the organic layer with refractive index n_{org} can be represented by a Hertz potential $\phi_{\infty}^{\mathrm{E,H}}(\mathbf{r})$ at an arbitrary position $\mathbf{r}$ [1]. By Fourier transform, Hertz potential of dipole $\phi_{\infty}^{\mathrm{E,H}}(\mathbf{r})$ can be decomposed into Hertz potentials of an infinite number of plane waves $\tilde{\phi}_{\infty,\pm}^{\mathrm{E,H}}(k_x,k_y)$. We also consider evanescent waves with imaginary k_z.

$$\phi_{\infty}^{\mathrm{E,H}}(\mathbf{r}) = \frac{1}{4\pi^2}\iint_{-\infty}^{\infty} \tilde{\phi}_{\infty,\pm}^{\mathrm{E,H}}(k_x,k_y)\, e^{i(k_x x + k_y y \pm k_z z)} dk_x dk_y \quad \#(\mathrm{S1.1})$$

$$k_z = \sqrt{n_{\mathrm{org}}^2 k_0^2 - \left(k_x^2 + k_y^2\right)} \quad \text{if } \left(k_x^2 + k_y^2\right) \le n_{\mathrm{org}}^2 k_0^2 \quad \#(\mathrm{S1.2})$$

$$k_z = i\sqrt{\left(k_x^2 + k_y^2\right) - n_{\mathrm{org}}^2 k_0^2} \quad \text{if } \left(k_x^2 + k_y^2\right) \ge n_{\mathrm{org}}^2 k_0^2 \quad \#(\mathrm{S1.3})$$

Here we color-code $\pm$ signs depending on their meaning: A red $\pm$ indicates the vertical propagation direction of a plane wave of interest, and a blue $\pm$ specify the vertical direction of the plane wave at the time of emission. Since the vertical propagation direction of a wave flips upon reflection, the two signs become opposite when a plane wave experiences an odd number of reflections.

Hertz potential of the plane wave from a light-emitting dipole with dipole moment $\mathbf{p} = p_0\hat{\mathbf{p}}$ is determined by its polarization, where $\hat{\mathbf{p}}$ is a unit vector specifying the dipole orientation [2]. For simplicity, we assume that $\hat{\mathbf{p}}$ exists on the *xz*-plane. Therefore, $\hat{\mathbf{p}} = (\sin\theta, 0, \cos\theta)$, where θ is the angle between the z-axis and the dipole orientation.

$$\tilde{\phi}_{\infty,\pm}^{\mathrm{E}}(k_x,k_y) = \frac{ip_0}{2}\left(\frac{\cos\theta}{k_z} \mp \frac{k_x \sin\theta}{k_x^2 + k_y^2}\right) \#(\mathrm{S1.4})$$

$$\tilde{\phi}_{\infty,\pm}^{\mathrm{H}}(k_x,k_y) = -\frac{ip_0\mu_0\omega}{2}\frac{k_y \sin\theta}{k_z(k_x^2 + k_y^2)} \quad \#(\mathrm{S1.5})$$

Electric field and magnetic field can be obtained from the Hertz potential of the plane wave.

$$\mathbf{k}_{\pm} = (k_x, k_y, \pm k_z) \#(\mathrm{S1.6})$$

$$\tilde{\boldsymbol{\phi}}_{\pm}^{E,H} = \left(0, 0, \tilde{\phi}_{\infty,\pm}^{E,H}\right) \#(\mathrm{S1.7})$$

$$\tilde{\mathbf{E}}_{\pm,\pm}^{\mathrm{TE}}(k_x, k_y) = -\omega \mathbf{k}_{\pm} \times \tilde{\boldsymbol{\phi}}_{\pm}^{H} \#(\mathrm{S1.8})$$

$$\tilde{\mathbf{E}}_{\pm,\pm}^{\mathrm{TM}}(k_x, k_y) = -\frac{1}{\epsilon\epsilon_0}\mathbf{k}_{\pm} \times \mathbf{k}_{\pm} \times \tilde{\boldsymbol{\phi}}_{\pm}^{E} \#(\mathrm{S1.9})$$

$$\mathbf{E}(\mathbf{r}) = \frac{1}{4\pi^2}\iint_{-\infty}^{\infty} \tilde{\mathbf{E}}_{\pm,\pm}^{\mathrm{TE,TM}}(k_x,k_y)\, e^{i(k_x x + k_y y \pm k_z z)} dk_x dk_y$$

$$= \frac{n_{\mathrm{org}}^2 k_0^2}{4\pi^2}\iint_{-\infty}^{\infty} \tilde{\mathbf{E}}_{\pm,\pm}^{\mathrm{TE,TM}}(u_x, u_y)\, e^{i n_{\mathrm{org}} k_0 (u_x x + u_y y \pm u_z z)} du_x du_y \quad \#(\mathrm{S1.10})$$

Here, $u = k/(n_{\mathrm{org}} k_0)$ is the normalized wavevector. By calculating Eq. S1.8 and Eq. S1.9, the electric field of a decomposed plane wave is obtained.

$$\tilde{\mathbf{E}}_{\pm,\pm}^{\mathrm{TE}}(u_x, u_y) = \frac{i p_0 \mu_0 \omega^2}{2} \frac{k_y \sin\theta}{k_z (k_x^2 + k_y^2)} \begin{pmatrix} -k_y \\ k_x \\ 0 \end{pmatrix}$$

$$= \frac{i p_0 k_0}{2 n_{\mathrm{org}} \epsilon_0} \frac{u_y \sin\theta}{u_z u_\parallel^2} \begin{pmatrix} -u_y \\ u_x \\ 0 \end{pmatrix}$$

$$= B\, \frac{u_y sin\theta}{u_z u_\parallel^2} \begin{pmatrix} -u_y \\ u_x \\ 0 \end{pmatrix} \#(\mathrm{S1.11})$$

$$\tilde{\mathbf{E}}_{\pm,\pm}^{\mathrm{TM}}(u_x, u_y) = -\frac{i p_0}{2 n_{\mathrm{org}}^2 \epsilon_0} \left(\frac{\cos\theta}{k_z} \mp \frac{k_x \sin\theta}{k_x^2 + k_y^2} \right) \begin{pmatrix} \pm k_x k_z \\ \pm k_y k_z \\ -k_\parallel^2 \end{pmatrix}$$

$$= \frac{i p_0 k_0}{2 n_{\mathrm{org}} \epsilon_0} \left(-\frac{\cos\theta}{u_z} \pm \frac{u_x \sin\theta}{u_\parallel^2} \right) \begin{pmatrix} \pm u_x u_z \\ \pm u_y u_z \\ -u_\parallel^2 \end{pmatrix}$$

$$= B \left(-\frac{\cos\theta}{u_z} \pm \frac{u_x \sin\theta}{u_\parallel^2} \right) \begin{pmatrix} \pm u_x u_z \\ \pm u_y u_z \\ -u_\parallel^2 \end{pmatrix} \#(\mathrm{S1.12})$$

$$B = \frac{i p_0 k_0}{2 n_{org} \epsilon_0} \quad \#(\mathrm{S1.13})$$

The complex electric field amplitude, $a_\pm$, is obtained by calculating the amplitude of the electric field unit vector in Eq. S1.12 and Eq. S1.13. In Table S1, we summarize the complex electric field amplitude, $a_\pm$, of the decomposed TE/TM polarized plane waves for three different dipole orientations. Value of $a_\pm$ for x and z-oriented dipoles are obtained by setting θ to 0 and $\pi/2$, respectively. In case of a y-oriented dipole, the value of $a_\pm$ is retrieved by applying the rotational symmetry to $a_\pm$ from the x-oriented dipole.

Table S1| Complex electric field amplitude of a plane wave for different dipole orientations and polarizations. The subscript $\pm$ is determined by the vertical propagation direction of the plane wave at the time of emission.

$B^{-1} \cdot a_{\pm}$	TE	TM
x-oriented dipole	$\frac{u_y}{u_z u_{\parallel}}$	$\pm \frac{u_x}{u_{\parallel}}$
y-oriented dipole	$-\frac{u_x}{u_z u_{\parallel}}$	$\pm \frac{u_y}{u_{\parallel}}$
z-oriented dipole	0	$\frac{u_{\parallel}}{u_z}$

S2. Visualization of diffraction matrices

To deal with diffraction, we rearrange the diffraction coefficients into a matrix form. Figure S1 illustrates the image plot of the absolute values of $\mathbf{R}_{-}$ coefficients of 0nm (planar) and 20nm-height corrugated OLED in Figure 3(a). In case of the planar OLED (Figure S1(a)), only the diagonal elements of the diffraction matrix have non-zero values. As the diagonal elements correspond to the reflection coefficients of the undiffracted rays, Figure S1(a) implies that diffraction and polarization conversion don't occur. However, if the boundary is corrugated, non-zero off-diagonal elements appear which implies the existence of diffraction occurring at the corrugated boundary. Nonzero values placed on the first and third quadrants show that polarization conversion occurs.

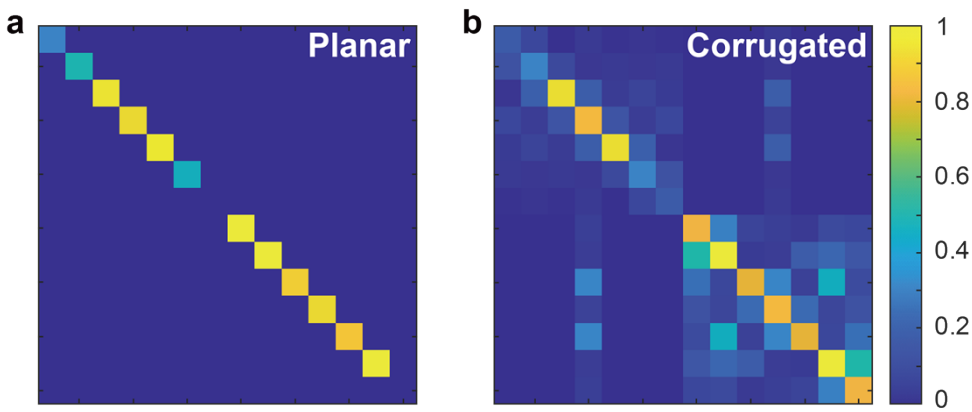

Figure S1| Visualization of diffraction matrices. (a), (b). Color plot of absolute values of diffraction matrix coefficients of planar **(a)** and corrugated **(b)** boundary interfaces.

S3. Relationship between the calculation time and DMM parameters

We performed LEE calculation with DMM while varying the number of Fourier orders n_{RCWA} and the number of sampled points in Brillouin zone, n_{BZ}. In Figure S2(a), the relationship between the calculation time and n_{RCWA} is plotted while fixing the value of n_{BZ} to 70. For large n_{RCWA}, the calculation time becomes proportional to $n_{\mathrm{RCWA}}^{1.8-2}$. In theory, the calculation time should be proportional to n_{RCWA}^{2}, because each dimension of the 2D matrix retained in the RCWA calculation proportional to n_{RCWA}. The actual calculation time deviates from the prediction due to calculation processes independent of n_{RCWA}. Also, high Fourier order matrix coefficients have near-zero values, so the computational cost is reduced.

In Figure S2(b), the relationship between the calculation time and n_{BZ} is investigated while fixing the n_{RCWA} to 20. For large n_{BZ}, the calculation time scales with $n_{\mathrm{BZ}}^{1.7-1.9}$. It agrees with the theoretical result n_{BZ}^{2}, determined by the total number of sampled points to perform integration.

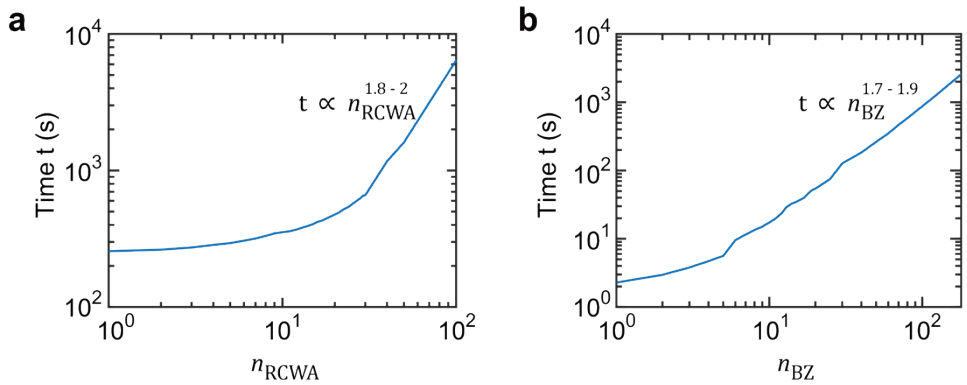

Figure S2| Required calculation time of DMM function of n_{RCWA} and n_{BZ}. (a) Calculation time of DMM is plotted as a function of **(a)** n_{RCWA} and **(b)** n_{BZ}. Value of n_{BZ}, and n_{RCWA} is fixed to 70 and 20, respectively.

S4. LEE convergence

To assure the convergence of DMM, we perform multiple calculations while varying n_{RCWA}. n_{BZ} is fixed to 150. LEE calculation result is plotted in Figure S3(a). As shown in Figure S3(a), LEE oscillates and converges to 15.89%. We also confirmed that LEE (Purcell factor) converges to the same value, 15.89% (1.268), even for n_{BZ} = 300.

In FDTD, we set the minimum mesh size to 3 nm × 3 nm × 3 nm and y-dimensional simulation size to 25 μm and calculate LEE by increasing the x-dimensional simulation size. LEE increases as x-dimensional simulation size increases. LEE (Purcell factor) converges to 15.96% (1.243). Therefore, the two methods quantitatively agree within 1% for LEE and 2% for Purcell factor.

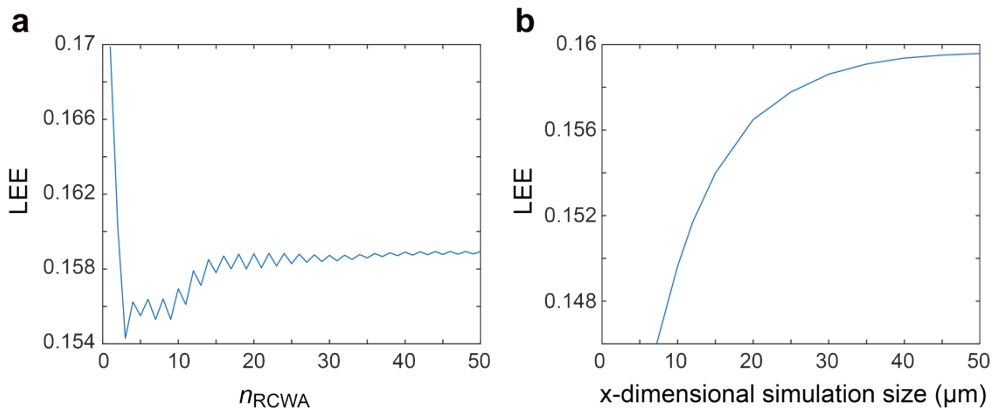

Figure S3| LEE convergence graph calculated by DMM and FDTD. (a) The convergence of DMM is examined by plotting LEE as a function of $\boldsymbol{n_{\mathrm{RCWA}}}$ ($\boldsymbol{n_{\mathrm{BZ}}}$ = 150). **(b)** LEE value calculated with FDTD is plotted as a function of x-dimensional simulation size. The minimum mesh size and y-dimensional simulation size are 3 nm × 3 nm × 3 nm and 25 **μm.** LEE converges to 15.89% and 15.96% in DMM and FDTD, respectively.

S5. Reduction of ripple-like feature by increasing simulation space size

In the main text, all far field pattern calculated from the FDTD simulation had ripple-like feature which is absent in DMM results. We speculated that the origin of this pattern was the finite simulation space. Hence, we perform FDTD simulations with different simulation configuration one OLED structure and demonstrate how the ripple-like features are affected. Color plots in Figure S4 are the simulated far-field intensity patterns obtained from FDTD simulation. The simulation space size varies from $5 \times 5\ \mu\text{m}$ to $25 \times 25\ \mu\text{m}$. As simulation space size increases, the far-field intensity pattern becomes sharper and the ripple-like feature fades away. As the ripple-like feature vanishes, calculated LEE converges to the value calculated by DMM. The calculated LEE of simulation space size $5 \times 5\ \mu\text{m}$ is 0.1409 thus its error rate is 11.72%. As simulation space size increases, the error rate decreases: (b) 6.62%, (c) 3.88%, (d) 2.20%, and (e) 1.25%.

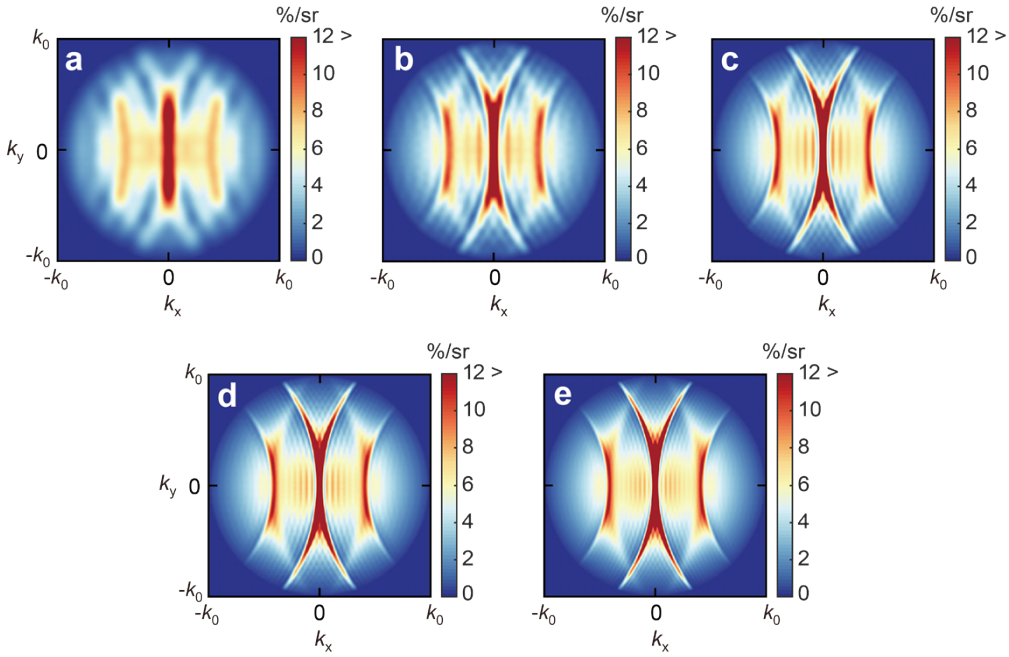

Figure S4| Far-field intensity pattern from different FDTD simulation space size. (a) – (e) Far-field emission pattern simulated by FDTD with simulation space size **(a)** 5 × 5 μm **(b)** 10 × 10 μm **(c)** 15 × 15 μm **(d)** 20 × 20 μm **(e)** 25 × 25 μm.

S6. Number of FDTD simulations required to simulate an emission plane.

Emission profiles from dipoles in different positions must be averaged out to calculate the emission profile in a corrugated OLED. We compare the averaged emission profile obtained from FDTD to emission profile obtained via analytical integration using DMM. Through the comparison, we determine the required number of FDTD simulations (Figure S5).

We average the emission profiles from dipoles placed in equal intervals along the emission plane. If the number of dipoles is N and the period of the grating is P, the distance between the two nearest dipoles is equal to the P/N. So, x_{dip}, the horizontal distance of dipole and top of the center of the grating, is set to nP/N, which n is integer from one to N. Figure S5 shows the RMS errors of two far-field intensity patterns, obtained by averaging and analytical integration. We calculate the RMS errors for two different corrugation height $\mathrm{h_{corr}}$: 20nm and 120nm. In case of $\mathrm{h_{corr}}$ = 120nm, the minimum distance between the dipole and the metallic slab becomes 5 nm. Therefore, a huge difference in far-field intensity pattern is found between the two cases when the horizontal position of the dipole is the center of the metallic slab and the center of the organic slab. The difference in far-field intensity pattern is high when the number of the dipole is low at high $\mathrm{h_{corr}}$. However, when emission pattern from more than seven of dipoles are averaged, the averaged emission pattern agrees with the emission pattern obtained through analytical integration within machine precision regardless of $\mathrm{h_{corr}}$. Since the periodic grating is symmetric, the far-field pattern of $x_{\mathrm{dip}} = nP/\mathrm{N}$ and $x_{\mathrm{dip}} = (\mathrm{N}-n)P/\mathrm{N}$ are also symmetric. Therefore, required FDTD simulations to assure convergence is 12 simulations, considering x, y, z dipole orientations.

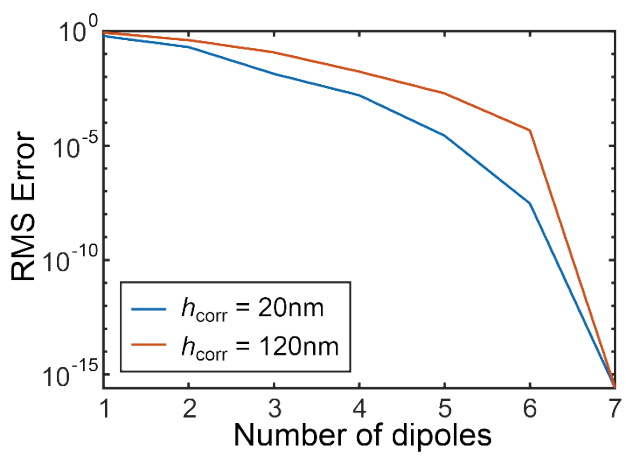

Figure S5| RMS error in the averaged far-field intensity pattern is plotted as a function of number of emission profiles used.

S7. Analytical integration

Since we deal with infinite number of incoherent emitters in the emission plane, it is possible to take an analytical integration on outcoupled power density $F_{\text{out}}(\mathbf{u})$ and $K_{\text{out}}(\mathbf{u})$ using DMM. To obtain $F_{\text{out}}(\mathbf{u})$, we need to calculate $a_{\text{top}}(\mathbf{u})$, which is related to the position of the dipole. We first represent Eq. 11. into a simpler form.

$$\mathbf{A}_{\text{top}} = \mathbf{Q}_{+}\mathbf{X}\mathbf{A}_{+} + \mathbf{Q}_{-}\mathbf{X}\mathbf{A}_{-} \quad \#(\text{S7.1})$$

$$\mathbf{Q}_{+} = (\mathbf{I} - \mathbf{C}_{-}\mathbf{C}_{+})^{-1}\mathbf{P}_{+} \quad \#(\text{S7.2})$$

$$\mathbf{Q}_{-} = (\mathbf{I} - \mathbf{C}_{-}\mathbf{C}_{+})^{-1}\mathbf{C}_{-}\mathbf{P}_{-} \quad \#(\text{S7.3})$$

Then, i^{th} element of $\mathbf{A}_{\text{top}}$ can be expressed by the equation below.

$$\mathbf{A}_{\text{top},i} = \sum_{j=-M}^{M} \mathbf{Q}_{+,ij}\mathbf{X}_{jj}\mathbf{A}_{+,j} + \mathbf{Q}_{-,ij}\mathbf{X}_{jj}\mathbf{A}_{-,j} \quad \#(\text{S7.4})$$

We can divide position-independent and position-dependent parameters by replacing matrix elements into values. We assume that the corrugated grating is periodic in x-direction and drop $e^{-ik_{y,m}y}$ for simplicity.

$$a_{\text{top}}(\mathbf{u}_i) = \sum_{j=-M}^{M} \left\{\mathbf{Q}_{+,ij}a_{+}(\boldsymbol{u}_j) + \mathbf{Q}_{-,ij}a_{-}(\boldsymbol{u}_j)\right\}e^{-ik_{x,j}x} \quad \#(\text{S7.5})$$

$$= \sum_{j=-M}^{M} V_{i,j}e^{-ik_{x,j}x} \quad \#(\text{S7.6})$$

We can calculate $|a_{\text{top}}(\mathbf{u}_i)|^{\mathbf{2}}$, which is related to F_{out} and K_{out}.

$$|a_{\text{top}}(\mathbf{u}_i)|^2 = |V_{i,-M}|^2 + \ldots + |V_{i,M}|^2 + \sum_{a\neq b} V_{i,a}^{*}V_{i,b}e^{i(k_{x,a}-k_{x,b})x} \quad \#(\text{S7.7})$$

By integrating $|a_{\text{top}}(\mathbf{u}_i)|^2$ with dx, we obtain the average normalized outcoupled plane wave power of incoherent dipoles.

$$< |a_{\text{top}}(\mathbf{u}_i)|^2 > = |V_{i,-M}|^2 + \ldots + |V_{i,M}|^2 + \frac{1}{P}\int_0^P dx \sum_{a\neq b} V_{i,a}^{*}V_{i,b}e^{i(k_{x,a}-k_{x,b})x} \quad \#(\text{S7.8})$$

Since $k_{x,a} - k_{x,b} = 2\pi/P \cdot (a-b)$, the one-period integration of $\sum_{a\neq b} V_{i,a}^{*} V_{i,b} e^{i(k_{x,a}-k_{x,b})x}$ is zero.

$$< |a_{\text{top}}(\mathbf{u}_i)|^2 > \; = |V_{i,-M}|^2 + \ldots + |V_{i,M}|^2 \; \#(\text{S7.9})$$

Therefore, analytical integration along the different dipole positions is obtained by calculating matrix elements of Eq. S7.9.

Similarly, $K(\mathbf{u}_i)$ in Eq. 6 can be represented in a simplified form.

$$K(\mathbf{u}_i) = \sum_{a=-M}^{M} W_{i,a} e^{-ik_{x,a}x} \cdot e^{ik_{x,0}x} \; \#(\text{S7.10})$$

$$< K(\mathbf{u}_i) > \; = \frac{1}{P}\int_0^P dx \sum_{a=-M}^{M} W_{i,a} e^{i(k_{x,0}-k_{x,a})x} \; \#(\text{S7.11})$$

Since the one-period integration of $e^{i(k_{x,0}-k_{x,a})x}$ is zero when $a \neq 0$, only $a = 0$ term survives.

$$< K(\mathbf{u}_i) > \; = W_0 \; \#(\text{S7.12})$$

Therefore, the total power emitted by the emitter inside the device (F) and the out-coupled light power that eventually escapes the device (F_{out}) can be calculated analytically. And finally, LEE and the Purcell factor of corrugated OLED with planar emission can be calculated.

S8. Convergence and calculation time of DMM and FDTD

We conduct a parameter sweep of n_{RCWA} and n_{BZ} to find proper calculation time that guarantees the convergence within 1% of ground truth value (Figure S6). Since two parameters, n_{RCWA} and n_{BZ}, both affects the convergence of LEE, we first fix n_{BZ} to 70 to investigate the influence of n_{RCWA}. As shown in Figure S6(a), we find that LEE converges below 1% when n_{RCWA} is over 16. Therefore, we set n_{RCWA} to 20. In Figure S6(b), we calculated LEE for different values of n_{BZ}. As shown in the graph, LEE stops oscillating when n_{BZ} is greater than 40. LEE at $n_{\mathrm{BZ}} = 40$ is 0.1576, which also agrees with the ground truth value within 1% error. Therefore, we set the appropriate conditions to confirm the convergence, which is $n_{\mathrm{RCWA}} = 20$ and $n_{\mathrm{BZ}} = 40$. In this case the measured calculation time is 185 s.

The simulation size and the minimum mesh size determines the accuracy and calculation time of a FDTD simulation. Figure S7(a) is a color plot of LEEs for different simulation space size. We change x and y dimension of the simulation space from 1 μm to 25 μm. The minimum mesh size is 3 nm × 3 nm × 3 nm. As shown in Figure S7(a), the x dimensional simulation size is more sensitive to LEE than y dimensional simulation size. So, we set the value of y dimensional simulation size to 25 μm.

To determine appropriate minimum mesh size, we calculate LEE and Purcell factors with different minimum mesh sizes with a fixed simulation space size of 5 μm × 5 μm. LEE and Purcell factors of various minimum mesh sizes and dipole orientations are summarized in Table S2. LEE and Purcell factor agrees with the ground truth value with error less than 1% when the minimum mesh size in the direction of dipole moment is 3 nm, while that of other directions are 5 nm.

With the minimum mesh size and the y dimensional simulation size determined, we calculate LEE and Purcell factor while tuning the x-dimension of the simulation space. In Figure S7(b), the average simulation times of corrugated OLEDs with x, y, z-oriented dipoles and calculated LEE are plotted. LEE converges within 1% when the simulation space in x is longer than 30 μm and the average simulation time is 11200 s.

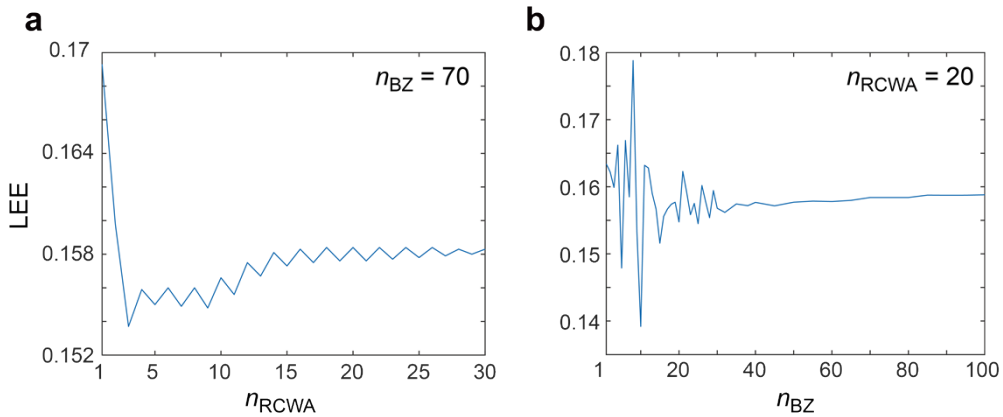

Figure S6| Effect of n_{RCWA} and n_{BZ} on LEE calculation using DMM. (a) A plot of LEE as a function of n_{RCWA} (n_{BZ} = 70). LEE converges within 1% when n_{RCWA} is greater than 16. **(b)** LEE calculation by increasing n_{BZ}. n_{RCWA} is fixed to 20. LEE converges within 1% when n_{BZ} is over 40.

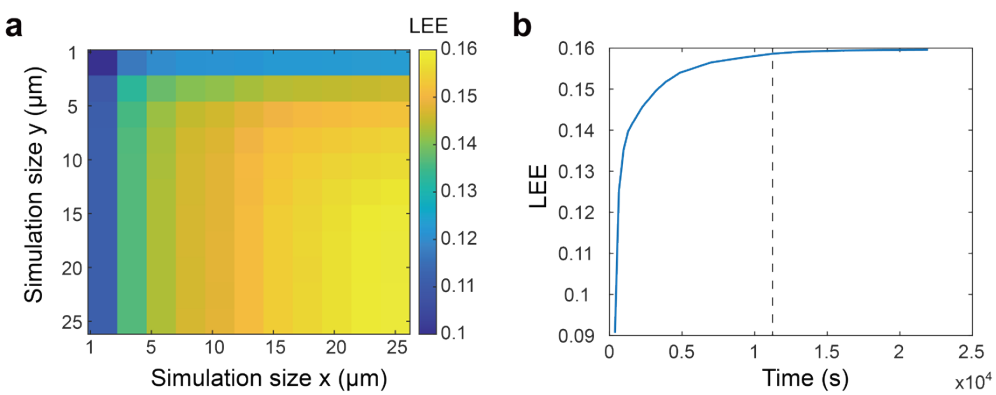

Figure S7| Effect of simulation size on LEE calculation in FDTD and calculation time. (a) A color plot of LEE as a function of x and y dimension of simulation size. The minimum mesh size is fixed to 3 nm × 3 nm × 3 nm. **(b)** LEE as a function of calculation time by increasing x dimension of simulation size. The y dimension of simulation size is fixed to 25 μm. LEE converges within 1% when x dimension of simulation size is greater than 30 μm and the calculation time is greater than 11200 s.

Table S2| Simulated LEE and Purcell factor with different minimum mesh sizes

x-oriented dipole minimum mesh size (x, y, z) (nm)	(3, 3, 3)	(4, 3, 3)	(5, 3, 3)	(6, 3, 3)	(3, 5, 3)	(3, 7, 3)	(3, 3, 5)	(3, 3, 7)	(3, 5, 5)
LEE	0.1897	0.1904	0.1921	0.1936	0.1898	0.1903	0.1896	0.1874	0.1898
Purcell factor	1.2063	1.2003	1.1884	1.1803	1.2051	1.2013	1.2029	1.1946	1.2017
y-oriented dipole minimum mesh size (nm)	(3, 3, 3)	(4, 3, 3)	(5, 3, 3)	(6, 3, 3)	(3, 5, 3)	(3, 3, 5)	(6, 3, 5)	(5, 4, 5)	(5, 3, 5)
LEE	0.2205	0.2209	0.2212	0.2217	0.2233	0.2206	0.2219	0.2219	0.2213
Purcell factor	1.1216	1.1184	1.1165	1.1133	1.1073	1.1153	1.1090	1.1089	1.1119
z-oriented dipole minimum mesh size (nm)	(3, 3, 3)	(4, 3, 3)	(5, 3, 3)	(3, 5, 3)	(3, 7, 3)	(3, 3, 5)	(5, 7, 3)	(5, 5, 4)	(5, 5, 3)
LEE	0.0355	0.0352	0.0350	0.0356	0.0358	0.0366	0.0352	0.3638	0.0362
Purcell factor	1.4115	1.4069	1.4044	1.4081	1.4002	1.3974	1.3932	1.4046	1.4066

S9. Flow chart of DMM

Flow chart of DMM is summarized in Figure S8. DMM procedure can be segmented into five processes: RCWA calculation, diffraction matrix generation, decomposition into plane waves, power fraction calculation in the reciprocal space, and finally, calculation of optical characteristics of corrugated LED. Average time consumption of each step is also denoted in the same diagram. RCWA calculation is consumes 174 s, which is 94% of whole DMM calculation. Overall remaining processes including diffraction matrix generation, dipole plane wave decomposition takes about 10 seconds. Therefore, if we update the grating-unrelated parameters like the dipole position/orientation, and the organic layer thickness, we can reduce the computation time required time to 5% of the original computation time.

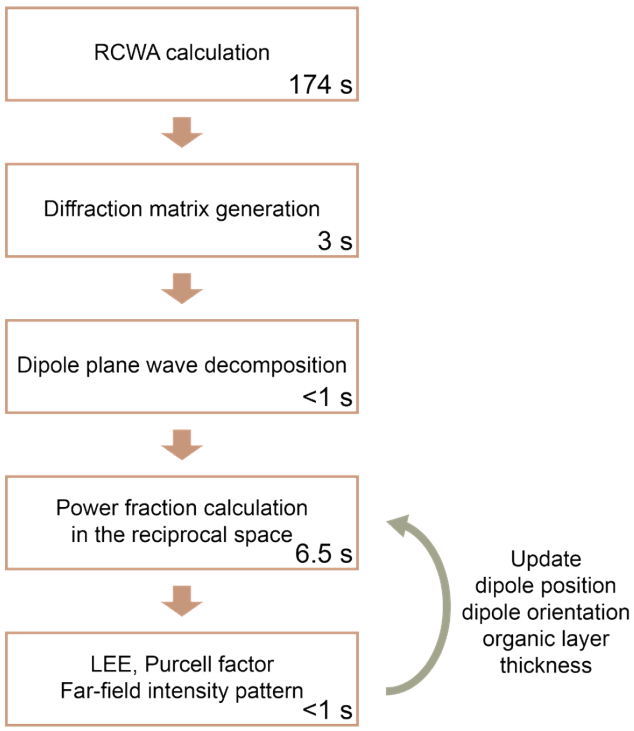

Figure S8| Flow chart of DMM. Computational time cost for each process is measured with parameters $\boldsymbol{n}_{\mathbf{RCWA}} =$ 20 and $\boldsymbol{n}_{\mathbf{BZ}} =$ 40.

S10. Exemplary Optimization with DMM

As described in Figure S8, DMM enables fast optimization of grating-unrelated parameters. Here, we optimize the value of h_{dip} and h_{org} through a full parameter sweep. Three different corrugation heights (0 nm, 20 nm, 50 nm) are selected as an example. The result of parametric sweep results is exhibited in Figure S9. The optimal value of h_{dip} and h_{org} are summarized in Table S3.

The optimized parameters of corrugated OLED are different to the optimized parameters of planar OLED, which means that it is impossible to get maximum LEE by adding a periodic corrugated layer into the optimized planar OLED.

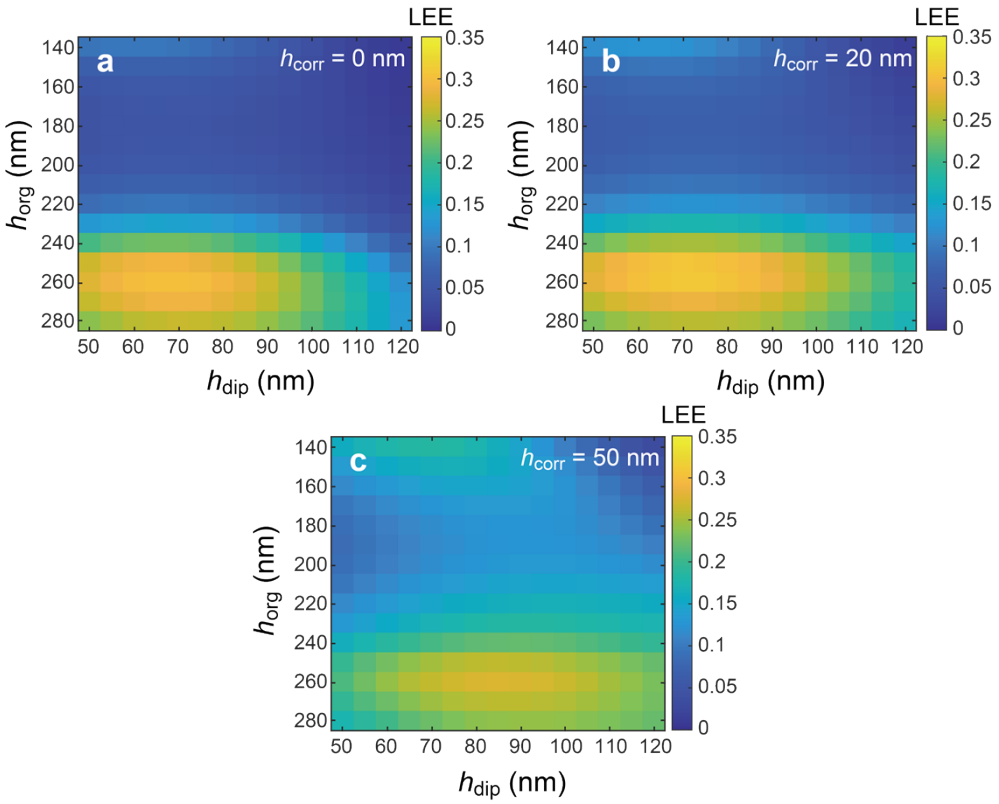

Figure S9| Optimization results of h_{dip} and h_{org} of planar and corrugated OLED. (a) – (c) The color plot displays the LEE values for: **(a)** Planar/uncorrugated OLED, **(b)** corrugation height of 20 nm corrugated, **(c)** 50 nm corrugated OLED, while changing h_{dip} from 50 nm to 120 nm, and h_{dip} from 140 nm to 280 nm.

Table S3| Optimal value of h_{dip}, h_{org} and optimized LEE

h_{corr}	h_{dip}	h_{corr}	Optimized LEE
0 nm	68 nm	258 nm	30.32%
20 nm	72 nm	261 nm	31.17%
50 nm	85 nm	258 nm	27.44%

S11. 2D DMM implementation

When a plane wave with in-plane wavevector $\mathbf{k}_{0,0}$ is incident to a 2D corrugation grating, diffraction occurs at the boundary and wavevector changes by the crystal momentum of the grating:

$$\mathbf{k}_{m,n} = \mathbf{k}_{0,0} + m\mathbf{G_1} + n\mathbf{G_2}, \mathbf{G_1} = \frac{2\pi}{P_1}\hat{x}, \mathbf{G_2} = \frac{2\pi}{P_2}\hat{y'} \quad \#(S11.1)$$

where P_1 is the period along the x direction and P_2 is the period along the y' direction with $\hat{y'} = \cos\phi\,\hat{x} + \sin\phi\hat{y}$. We assume that $\hat{y'} = \hat{y}$ in this section for simplicity. We may group planewaves with wavevector $\mathbf{k}_{m,n}$ for integer m and n. Since the corrugation grating is 2D, if we visualize the in-plane wavevectors of diffracted plane waves to the reciprocal space, its trivial representation would be 2D matrix. However, in order to transform the diffraction coefficients and generate the diffraction matrices, we flatten the matrix into a vector. By flattening, we obtain the $M'N' \times 1$ vector instead of $M' \times N'$ matrix ($M' = 2M + 1, N' = 2N + 1$, where M and N are the number of diffracted orders retained in the calculation). The $\tilde{\mathbf{E}}^{\mathbf{r}}$ representation in 2D grating version is shown below.

$$\tilde{\mathbf{E}}^{\mathbf{r}}[N'm + n] = \tilde{\mathbf{E}}_{\mathbf{r}}(\mathbf{k}_{m,n}) \quad \#(S11.2)$$

$$-M \le m < M, \; -N \le n < N, \qquad m \text{ and } n \text{ is integer} \quad \#(S11.3)$$

The remaining part of 2D DMM is identical to 1D DMM.

S12. 2D DMM accuracy

We discuss how DMM performs well with 2D corrugated OLED in terms of accuracy. Color plots in Figure S10 are the far-field light intensity distribution for different dipole positions. Far-field light intensity distributions calculated by DMM displayed in Figure S10(d) – (f) and far-field light intensity distributions calculated by Lumerical FDTD solver displayed in Figure S10(g) – (h) match well each other.

Along with the far-field image, we utilize LEE and the Purcell factor as an indicator for accuracy of DMM and FDTD. The calculation results are summarized in Table S4. The ~1% normalized discrepancy in LEE and the ~3% normalized discrepancy in Purcell factor are shown.

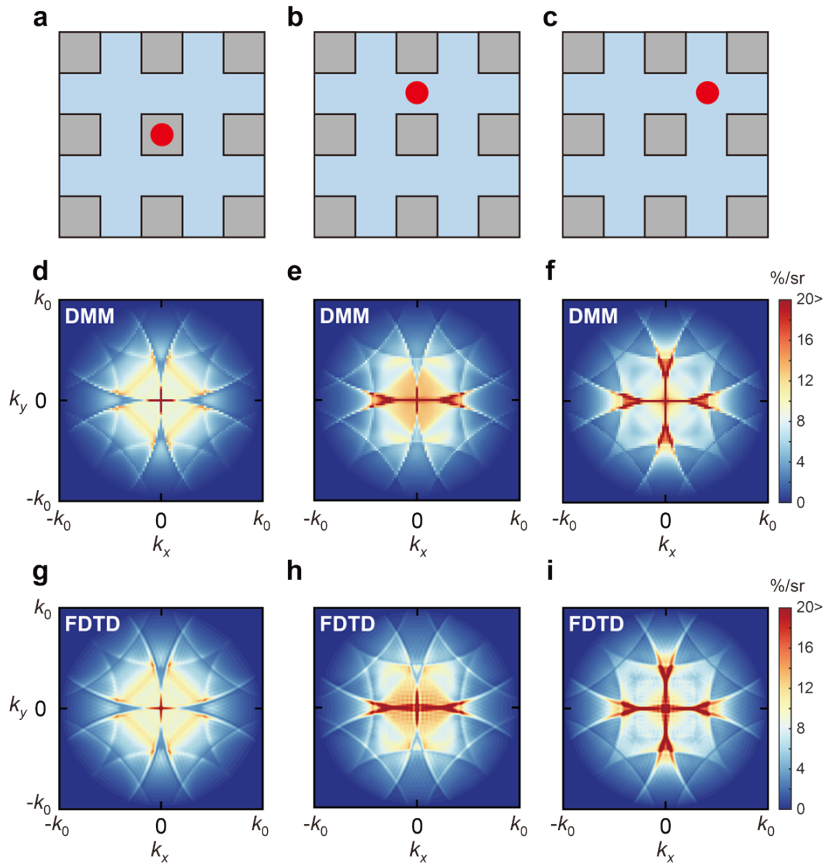

Figure S10| Comparison of 2D DMM and FDTD. (a) – (c) The simulation conditions of 2D corrugated OLEDs. The horizontal position of the light-emitting dipole is **(a)** center of metallic slab, **(b)** center of metallic slab, **(c)** center of metallic slab. **(d) – (i)** Corresponding color plots of far-field intensity patterns calculated by **(d-f)** DMM and **(g-i)** FDTD.

Table S4| LEE and Purcell factor calculated by DMM and FDTD

Figure	LEE (DMM)	LEE (FDTD)	Purcell factor (DMM)	Purcell factor (FDTD)
a	16.15%	16.04%	0.9922	0.9714
b	17.55%	17.67%	1.2850	1.2571
c	18.28%	18.29%	1.1414	1.1125

References

1. Lukosz, W. and R.E. Kunz, *Light-Emission by Magnetic and Electric Dipoles Close to a Plane Interface .1. Total Radiated Power.* Journal of the Optical Society of America, 1977. **67**(12): p. 1607-1615.
2. Lukosz, W., *Theory of Optical-Environment-Dependent Spontaneous-Emission Rates for Emitters in Thin-Layers.* Physical Review B, 1980. **22**(6): p. 3030-3038.